

RESEARCH ARTICLE

10.1029/2018JB016054

Key Points:

- Deformation during the 2010–2011 unrest at Taal volcano is explained by inflation of a shallow magmatic source
- Numerical models of viscoelastic deformation revealed rheological properties that fit the local geologic setting
- Surface deformation effects from the variability of Arrhenius parameters were demonstrated for different volcanic settings

Supporting Information:

- Supporting Information S1
- Data Set S1

Correspondence to:

A. M. Morales Rivera,
amorales@rsmas.miami.edu

Citation:

Morales Rivera, A. M., Amelung, F., Albino, F., & Gregg, P. M. (2019). Impact of crustal rheology on temperature-dependent viscoelastic models of volcano deformation: Application to Taal volcano, Philippines. *Journal of Geophysical Research: Solid Earth*, 124, 978–994. <https://doi.org/10.1029/2018JB016054>

Received 2 MAY 2018

Accepted 21 NOV 2018

Accepted article online 23 NOV 2018

Published online 25 JAN 2019

Impact of Crustal Rheology on Temperature-Dependent Viscoelastic Models of Volcano Deformation: Application to Taal Volcano, Philippines

A. M. Morales Rivera^{1,2} , F. Amelung¹ , F. Albino^{1,3} , and P. M. Gregg⁴ 

¹Rosenstiel School of Marine and Atmospheric Science, University of Miami, Miami, FL, USA, ²Now at Chesapeake Energy Corporation, Oklahoma City, OK, USA, ³Now at School of Earth Sciences, University of Bristol, Bristol, UK, ⁴Department of Geology, University of Illinois at Urbana-Champaign, Champaign, IL, USA

Abstract We use ALOS-1 interferometric synthetic aperture radar data spanning the period of 2007–2011 to obtain time-dependent ground deformation data over Taal caldera related to the 2010–2011 volcanic unrest, which did not lead to an eruption. We employ finite element models that account for subsurface thermomechanical properties to test for viscoelastic deformation. We also examine the variability of crustal rheological parameters of the temperature-dependent Arrhenius formulation for viscosity, to investigate the effects on surface deformation. Deformation at Taal is observed to be time dependent and explained by a linear rate of pressure increase in a shallow magma reservoir at 5-km depth within a hot and viscoelastic upper crust. The best-fitting rheological properties of the local setting are consistent with either a felsic or hydrothermally altered uppermost crust. We show the significantly different effects that the variation of rheological parameters has on surface deformation, highlighting the importance of incorporation into future studies of deformation at different volcanic settings.

1. Introduction

Ground deformation resulting from magma movement toward the surface is one of the key observations needed for forecasting volcanic eruptions (e.g., Sparks, 2003). Geodetic observations can provide constraints on changes in pressure and volume of magma bodies (e.g., Lisowski, 2006), which could be used to estimate potential volumes of eruptive material and occurrence of magma reservoir failure. However, it can be difficult to determine whether detected ground deformation is due to instantaneous pressure changes in a magma reservoir or due to delayed deformation of the surrounding host rock, or both (e.g., Segall, 2016). To distinguish between these processes, knowledge is required of the rheological properties of the host rock (Currenti & Williams, 2014; Hurwitz et al., 2009), which will control how the Earth's surface deforms in response to magma reservoir pressurization at depth.

Rheological properties such as yield strength, viscosity, temperature, and composition (McBirney & Murase, 1984) can be represented with viscoelastic deformation modeling. Viscoelastic models have been extensively applied to volcano deformation studies (e.g., Bonafede et al., 1986; Dragoni & Magnanensi, 1989; Jellinek & DePaolo, 2003), providing important observations about crustal strain dependency to mechanical and rheological variations at different types of volcanoes (e.g., stratovolcanoes, Hickey et al., 2015; shields, Masterlark et al., 2010; calderas, Hickey et al., 2016; Newman et al., 2006) with magmatic systems of different geochemical compositions (e.g., from basaltic, Del Negro et al., 2009; to felsic, Le Mével et al., 2016) and varying thermal gradients (de Silva & Gregg, 2014). Moreover, viscoelastic models have also provided insights into eruption triggering mechanisms from small volcanic systems to catastrophic caldera forming eruptions (Gregg et al., 2012).

Recent viscoelastic models of volcano deformation have used the Arrhenius formulation (see section 3.3.3) to estimate the viscosities of the medium (e.g., Gregg et al., 2012; Hickey et al., 2015), employing commonly used variables within the formulation that are potentially representative of the composition and temperatures of the subsurface, without full exploration of their potential values. Understanding the possible variations within these parameters along with their implications is critical to depict realistic rheological scenarios. It is also crucial for future studies that aim to understand crustal deformation, magma reservoir failure, intrusion propagation, and eruption forecasting.

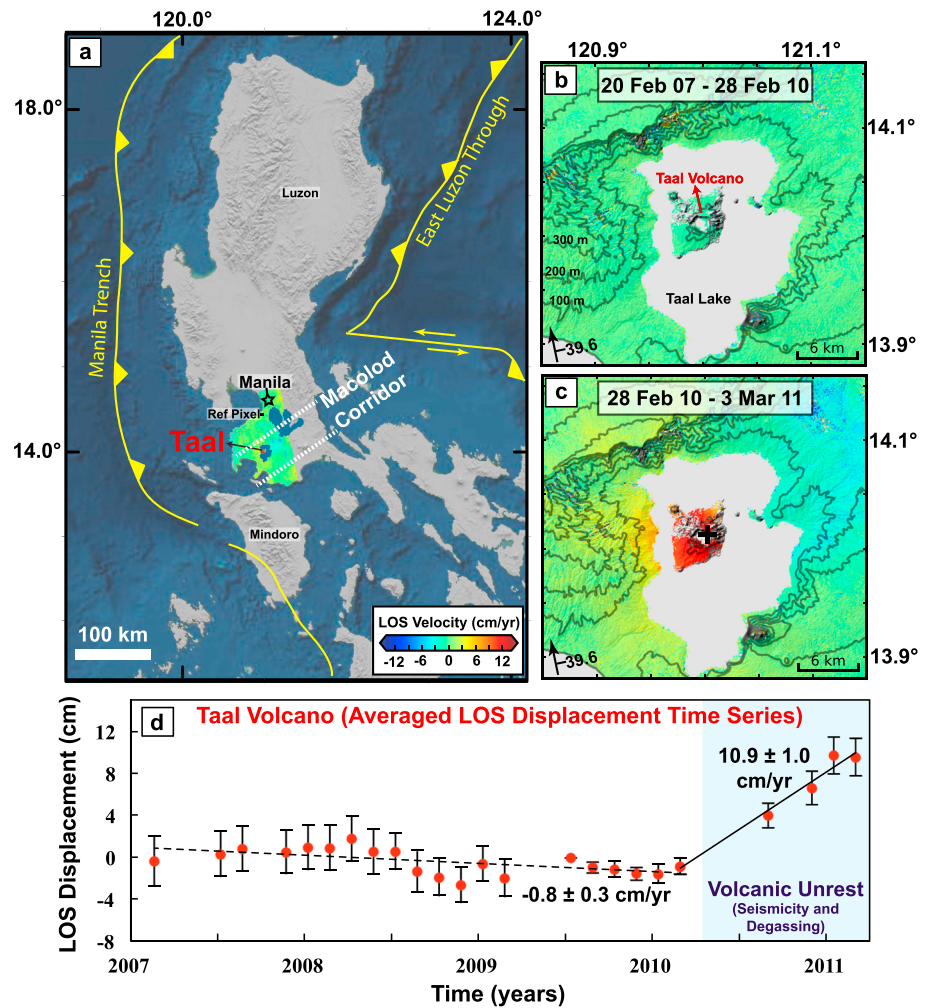


Figure 1. (a) Location of Taal caldera within the Philippines, showing simplified tectonic features and averaged line-of-sight (LOS) velocity map during the deforming period. (b, c) Averaged LOS velocity maps over Taal volcano for the given time periods. Arrows: The satellite flight direction. Black bars and numbers perpendicular to the arrows: Satellite look direction with incidence angle. Black cross: Best-fitting analytical point source location (Figure S9). (d) Averaged LOS displacement time series over Taal volcano. Black solid/dashed line: Best-fitting linear regression for different time periods with the corresponding deformation rate. Error bars: Standard deviation for all the coherent points within Taal volcano at each epoch. Blue-shaded area: Period of volcanic unrest.

In this study, we employ thermomechanical models of shallow volcanic systems to investigate how host rocks with distinct viscosity end members from the Arrhenius formulation affect the response of the Earth's surface due to magma reservoir pressurization. We apply the models to the 2010–2011 unrest at Taal volcano, for which deformation was detected with the interferometric synthetic aperture radar (InSAR) technique, to determine which rheological parameters are most appropriate to reproduce the observed surface deformation.

2. Taal Caldera and the 2010–2011 Unrest

Taal caldera is located within the Macolod Corridor in the Philippines (Figure 1a), a tectonically complex region characterized by active volcanism, crustal thinning, faulting, and block rotations (e.g., Galgana et al., 2014). The caldera is partially filled with the water body that forms Taal Lake (maximum water depth of ~160 m reported by the Philippine Institute of Volcanology and Seismology), and within the lake lies the active volcanic complex (Volcano Island or Taal Volcano, 311 m), consisting of >40 vents of which the

largest is the main crater (Delos Reyes et al., 2018). Part of the main crater (~1 km radius) is filled by an 80-m deep lake (Delmelle et al., 1998).

Recent eruptive products from Taal volcano have been predominantly basaltic to andesitic in composition (e.g., Lowry et al., 2001). Although Taal has not erupted since 1977, several episodes of unrest have intermittently occurred since 1992, as noted by changes in deformation, seismicity, and degassing (Arpa et al., 2013; Bartel et al., 2003). Given the high population density within proximity (>700,000 people within a 10-km radius; Global Volcanism Program, 2013), Taal volcano is one of the best monitored volcanoes in the Philippines.

PHIVOLCS reported several anomalous changes at Taal from April 2010 to June 2011, including increased seismicity, degassing, total magnetic field, water and ground temperatures, and inflation observed by precise leveling measurements (Arpa et al., 2013; Maeda et al., 2013). We report the signal observed at Taal with InSAR during this unrest period and test crustal rheological end members by thermomechanical deformation modeling.

3. Data and Methods

3.1. InSAR

Our data set (Table S1 in the supporting information) consists of 50 SAR scenes from two frames of ascending track 449 acquired between February of 2007 and March of 2011 by the ALOS-1 satellite of the Japan Aerospace Exploration Agency. We used an unweighted inversion approach to obtain the line-of-sight (LOS) displacement history and averaged LOS velocities from the generated network of interferograms. Further details on the InSAR data set, processing approach, and quality assessment of the displacement time series are found in the supporting information (Texts S1 and S2; Berardino et al., 2002; Chen & Zebker, 2001; Goldstein & Werner, 1998; Pepe & Lanari, 2006; Rosen et al., 2004; Werner et al., 2000).

3.2. Analytical Point Source Model

We use geophysical inverse methods to find the best-fitting point source solution within an elastic half-space (Mogi, 1958). The data are the generated InSAR LOS displacements (during the deforming period; Figure 1c), sampled using uniform grids to reduce the number of data points (each grid dimension was 300 m × 307 m). The InSAR data were weighted equally. We solve the inverse problem using a Monte-Carlo-based Gibbs sampling algorithm (Brooks & Frazer, 2005; Morales Rivera et al., 2016) with 100,000 sweeps to sample the posterior probability density function and find the optimal solution that yields the lowest root-mean-square error (RMSE). The solution was used as the basis for selecting the source location in the numerical models.

3.3. Finite Element Numerical Models

We expand on the numerical formulations and model setups from the benchmarked approach of Gregg et al. (2012) to develop 2-D axisymmetric finite element models (FEMs) using COMSOL Multiphysics software (<https://www.comsol.com>; a COMSOL.mph file with the model is provided in Data Set S1 of the supporting information). We used the solid mechanics module in conjunction with the heat transfer module to solve for the time- and temperature-dependent deformation.

3.3.1. Model Setup, Geometry, and Mesh

The magma reservoir is represented as a single pressurized spherical void within a viscoelastic medium, where an initial state of stress (lithostatic) between the magma reservoir and the surrounding medium is assumed to be in equilibrium (e.g., Hickey et al., 2013). The extents of the model space are 35 km × 35 km. We exclude the topography and assume a flat surface, as the summit of Taal volcano is only 300 m above sea level and topographic effects are negligible for our modeling application due to the low slope of the volcano (e.g., Cayol & Cornet, 1998; Masterlark, 2007).

The finite element mesh contains 1,266 tetrahedral elements, with a higher mesh density around the magma reservoir. The initial settings and boundary conditions of the models include (1) a freely deformable top surface, (2) rollers on the right lateral and bottom surfaces (to prevent deformation perpendicular to these boundaries), (3) axial symmetry and zero displacement on the left-lateral surface, and (4) a boundary load applied to the walls of the source cavity (Gregg et al., 2012; Figure 2).

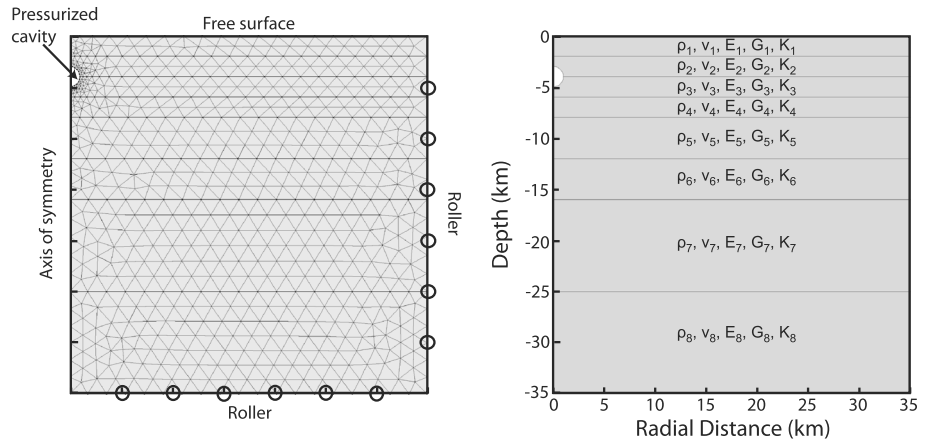


Figure 2. (left) Two-dimensional model setup, finite element mesh, and boundary conditions. Left boundary: Axial symmetry condition; right and bottom boundaries: Roller condition; top surface and pressurized cavity boundaries: Freely deformable condition. (right) Distribution of seismically constrained elastic material properties (Table 1).

We assume a fixed source radius of 1 km, in agreement with Galgana et al. (2014), who suggest that the radius of Taal volcano's main crater roughly represents that of the magma reservoir (e.g., Lipman, 1997; Roche et al., 2000). We center the pressurized spherical void (McTigue, 1987) at depths of 2, 3, 4, and 5 km, to cover the depth range of the best-fitting analytical solution (3.1 ± 2 km for 2 standard deviations; see section 4.1 and Table S4). We did not consider a source at 1-km depth, because it does not satisfy the Mogi requirement of a source depth greater than the source radius.

We assume instantaneous pressurization and apply 10, 20, 30, 40, and 50 MPa in excess of the lithostatic pressure along the spherical cavity boundary. The excess pressure is hereinafter referred to as overpressure. The instantaneous pressurization assumption ignores that magma influx is gradual and that the viscoelastic contribution from early pressurization decays faster, but is a common assumption in volcanic deformation modeling studies because the pressure buildup rate is not known.

We then evolved the model to consider linearly increasing rates of pressure change of 10, 20, 30, 40, and 50 MPa during 185, 277, 323, and 369 days (four time steps defined by InSAR data coverage in section 3.3.5). The actual rate of pressure change can depend on different nonlinear processes occurring within the magma reservoir (e.g., from new magma input, differentiation of magma in the reservoir, or exsolution and trapping of gases in the reservoir; Lisowski, 2006), which cannot be constrained with our data.

For both instantaneous and linear pressure models, we assume that magma reservoir overpressure is less than failure overpressure because an eruption did not occur. The study by Albino et al. (2018) supports that the tested range of overpressures does not lead to rupture or eruption under certain pore pressure conditions of the host rock, the latter being commonly unknown in volcanic systems.

3.3.2. Elastic Properties

We consider elastic heterogeneity (vertical) in our models for a more realistic representation of the subsurface. We used the 1-D seismic velocity model of You et al. (2013) for Taal caldera in order to delineate the mechanically heterogeneous layers (Figure 2), noting that elastic homogeneity would provide similar results in terms of surface displacement due to the low resolution of the seismic velocity model (Text S3). We infer the density (ρ), Poisson's Ratio (ν), and seismic Young's Modulus (E) from the P wave (V_p) and S wave (V_s) velocities, using the empirical relationships (Brocher, 2005):

$$\rho \left(\frac{\text{g}}{\text{cm}^3} \right) = 1.6612V_p - 0.4721V_p^2 + 0.0671V_p^3 - 0.0043V_p^4 + 0.000106V_p^5$$

$$\nu = 0.5 \left[\left(\frac{V_p}{V_s} \right)^2 - 2 \right] / \left[\left(\frac{V_p}{V_s} \right)^2 - 1 \right]$$

$$E = \left[V_p^2 \rho (1 + \nu) (1 - 2\nu) \right] / (1 - \nu)$$

and obtain the seismic shear modulus (G), and seismic bulk modulus (K) using:

Table 1
Elastic Parameters Estimated Using 1-D Seismic Velocities From You et al. (2013)

| Z (km) | ρ (kg/m ³) | ν | E (GPa) | G (GPa) | K (GPa) |
|------------------|-----------------------------|--------|---------|---------|---------|
| 1 to -2 (-2) | 2,437 | 0.2294 | 19.64 | 7.99 | 12.09 |
| -2 to -4 (-4) | 2,493 | 0.2099 | 24.67 | 10.20 | 14.18 |
| -4 to -6 (-6) | 2,558 | 0.2071 | 30.26 | 12.53 | 17.22 |
| -6 to -8 (-8) | 2,700 | 0.2495 | 39.46 | 15.79 | 26.26 |
| -8 to -12 (-12) | 2,818 | 0.3036 | 42.97 | 16.48 | 36.46 |
| -12 to -16 (-16) | 2,880 | 0.2270 | 55.68 | 22.69 | 33.99 |
| -16 to -25 (-25) | 3,009 | 0.2730 | 60.98 | 23.95 | 44.77 |
| -25 to -35 (-35) | 3,305 | 0.2763 | 84.29 | 33.02 | 62.80 |

Note. The reported Young's modulus, shear modulus, and bulk modulus are half of the seismic moduli (See section 3.3.2).

$$K = E/[3(1-2\nu)]$$

$$G = E/[2(1+\nu)]$$

We follow Gudmundsson (1990) and Hickey et al. (2016) by using half the seismic moduli in the models (Table 1) to account for the fact that the moduli determining the response of the Earth surface to magma reservoir pressurization are lower than the moduli determining the propagation speed of the seismic waves (e.g., Albino et al., 2018; Gudmundsson, 1990; Wauthier et al., 2012; Zhao et al., 2016). The relationship between the different types of moduli, which are sometimes referred to as static and dynamic moduli, are more complex (Adelinet et al., 2010; Ciccotti & Mulargia, 2004). But our approximation is acceptable because they are within reported ratios ranging from 0.11 to 0.67 for common extrusive rocks (e.g., Gudmundsson, 1990).

3.3.3. Viscous Properties

Viscosity is mainly used to determine the time-dependent deformation (section 3.3.4). We use a temperature-dependent viscosity (η) calculated from the Arrhenius formulation:

$$\eta = A_D \exp^{(E_A/R_b T)}$$

where A_D is the Dorn parameter (also called preexponential factor), E_A is the activation energy, R_b is the universal gas constant, and T is the temperature distribution calculated from the steady state heat conduction equation (e.g., Gregg et al., 2012). The Dorn parameter and the activation energy are constants for a given material, which have been experimentally derived for common rock types and minerals (e.g., Kirby & Kronenberg, 1987; Ranalli & Murphy, 1987) to determine the relationship between temperature and viscosity of different materials. In the following analysis we focus on testing the variables within this formulation (Dorn parameter, activation energy, and temperature distribution) in order to define viscosity end members and examine the response of the Earth's surface due to pressurization of a magma reservoir for different rheological configurations.

Compositional Model. The composition of the upper crust is generally represented as dry and wet granite to quartzite (Meissner & Tanner, 1992), but the Philippine Archipelago is built upon oceanic arcs, probably of diorite to amphibolite crustal composition (Vogel et al., 2006). Therefore, we used activation energy values of 106 kJ/mol (E_{A1}) and 219 kJ/mol (E_{A2}), respectively equivalent to a felsic and intermediate crust (Kirby & Kronenberg, 1987). The Dorn parameter was also varied to represent a felsic or intermediate crust, respectively represented by values of 5×10^9 (A_{D1}) and 2×10^{13} Pa s (A_{D2} ; Ranalli & Murphy, 1987). The combination of these parameters results in four crustal compositional models that were used in the analysis: $E_{A1} A_{D1}$, $E_{A1} A_{D2}$, $E_{A2} A_{D1}$, and $E_{A2} A_{D2}$.

Temperature Model. For each of the four crustal compositional models we considered two steady state temperature distributions, representing end members for shallow volcanic systems: (1) a cool magmatic source within a cool host rock (herein referred to as the cold model), and (2) a hot magmatic source within a hot host rock (herein referred to as the hot model).

The steady state temperature distributions were calculated using a surface temperature of 304 K (Arpa et al., 2013), a magma temperature range of 973 K for the cold model and 1673 K for the hot model (respectively representing dacites to basalts, covering the range of magmatic products from Taal; Miklius et al., 1991), and the geothermal gradients that are discussed in the following (Figure 3).

We use for the hot model geothermal gradients of 100 K/km for the upper 4 km and of 35 K/km for greater depth, and for the cold model a gradient of 15 K/km (Table 2). Thermal gradients generally range from 15 to 50 K/km (e.g., Rothstein & Manning, 2003). Long-lived calderas with extensive hydrothermal and magmatic systems have been suggested to have high geothermal gradients in the shallow crust (e.g., Yellowstone; Morgan et al., 1977) that can significantly alter stress and strain distributions and therefore the overall volcano deformation (Gaeta et al., 1998). The high temperatures of the shallow crust can be explained by recent heat transfer from the magmatic source into the hydrothermal system or by the long-lived thermal legacy from frequent magmatic activity. The gradient used in the hot model

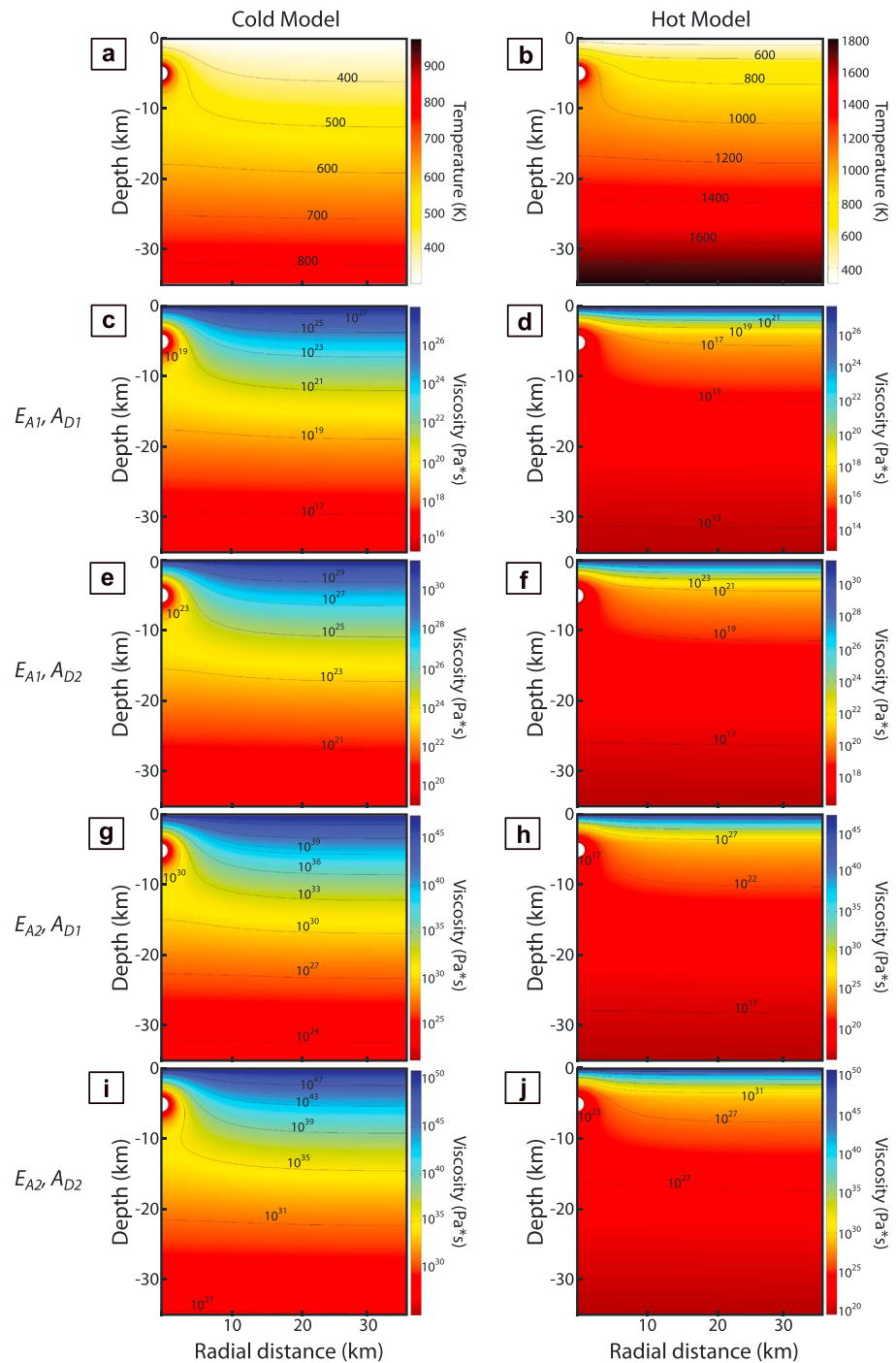


Figure 3. (a, b) Steady state temperature distribution for the cold and hot models with a spheroidal source (1-km radius) centered at 5-km depth, solved from the initial thermal boundary conditions and heat conduction parameters. (c–j) Viscosity distribution calculated from the Arrhenius formulation for the four crustal parameters (E_{A1} , E_{A2} , A_{D1} , and A_{D2} ; Table 2) combinations and the temperature distributions of (a) and (b).

for the upper 4 km is supported by local temperature estimates $>200\text{ }^{\circ}\text{C}$ ($>473\text{ K}$) of the extensive hydrothermal reservoir at Taal (Delmelle et al., 1998) and by the presence of a conductive zone down to 4-km depth (Yamaya et al., 2013). The geothermal gradient of the hot model for greater depths supports the expected temperatures at the approximated Moho depth of 34 km within this region of

Table 2
Model Parameters

| Parameter | Description | Value | Unit |
|-----------|---------------------------|--|-------------------|
| Fixed | | | |
| k | Thermal conductivity | 4 | W/(m K) |
| C_p | Heat capacity | 1150 | J/(kg K) |
| T_S | Surface temperature | 304 | K |
| R | Universal gas constant | 8.314 | J/(mol K) |
| R_c | Source radius | 1 | km |
| E | Young's modulus | Table 1 | GPa |
| G | Shear modulus | Table 1 | GPa |
| K | Bulk modulus | Table 1 | GPa |
| ν | Poisson's ratio | Table 1 | — |
| ρ | Density | Table 1 | kg/m ³ |
| Variable | | | |
| H_c | Depth to Source Center | 2, 3, 4, 5 | km |
| OP | Source Pressure | 10, 20, 30, 40, 50 | MPa |
| dT/dH_c | Geothermal gradient | 15 ^a , 35 ^b , 100 ^c | K/km |
| T_{MC} | Magma chamber temperature | 973 ^a , 1673 ^d | K |
| A_{D1} | Dorn parameter 1 | 5×10^9 | Pa s |
| A_{D2} | Dorn parameter 2 | 2×10^{13} | Pa s |
| E_{A1} | Activation energy 1 | 106 | kJ/mol |
| E_{A2} | Activation energy 2 | 219 | kJ/mol |
| η | Viscosity | See equation 6 | Pa s |
| τ | Relaxation time | See equation 7 | days |

^aCold model. ^bHot model for depths deeper than 4 km. ^cHot model for depths shallower than 4 km. ^dHot model.

the Philippines (Besana et al., 1995). The geothermal gradient chosen for the cold model supports the possibility of crustal cooling within shallow volcanic systems by water from shallow aquifers (e.g., Stolper et al., 2009) or by hydrothermal circulation (e.g., Morgan & Chen, 1993).

For the calculation of the steady state temperature distribution, we use the thermal conductivity (Clauser & Huenges, 2013) and heat capacity (Waples & Waples, 2004) values reported in Table 2. Their uncertainties are negligible for our calculation, because calderas are long lived and they would only affect the time it takes for heat to conduct (Hickey et al., 2015).

3.3.4. Viscoelastic Forward Models

The models were built to represent a medium with a Standard Linear Solid viscoelastic arrangement (Christensen, 1971), which have an instantaneous elastic response (used to evaluate deformation in an elastic medium) followed by a viscoelastic response that is dependent on the characteristic relaxation time (τ) of (Del Negro et al., 2009; Gregg et al., 2012):

$$\tau = \left(\frac{\eta}{G_0\mu_1} \right) * \left(\frac{3K + G_0}{3K + G_0\mu_0} \right)$$

where μ_0 and μ_1 are the fractional moduli and equal to 0.5.

Taking the previously described rheological configurations and parameters (summarized in Table 2), we built a total of eight model classes representing possible viscosity distributions at Taal (crustal

compositional models $E_{A1} A_{D1}$, $E_{A1} A_{D2}$, $E_{A2} A_{D1}$, and $E_{A2} A_{D2}$ with the two temperature distribution end members; Figure 3).

3.3.5. Approach to Determine the Best-Fitting Numerical Model

Our data only had four dates within 1 year with measured deformation (Figure 1); therefore, the data-model comparisons were done at the time steps defined by the period between InSAR acquisition dates with evident displacement. These time steps are as follows: (1) 185 days (28 February 2010 to 31 August 2010), (2) 277 days (28 February 2010 to 1 December 2010), (3) 323 days (28 February 2010 to 16 January 2011), and 369 days (28 February 2010 to 3 March 2011).

Because our FEMs are 2-D axisymmetric, we averaged nine InSAR displacement transects at each time step for the data-model comparisons. The nine transects radially extend an average of 19.5 km from the surface location directly above the analytical point source toward the southwest to well cover the deforming area, including that observed to the west of Volcano Island (for transect locations see Figure S7 in the supporting information). The orientations of the transects were chosen only toward the southwest, because it best captures the spatially broad deformation signal and because of better data coherence, as compared to other orientations. We have converted the LOS displacements into vertical displacements (Hanssen, 2001), assuming negligible horizontal ground displacement and an incidence angle of 39.6°.

We first ran the viscoelastic and elastic models (section 3.3.4) using the instant pressure assumption (section 3.3.1) and compared the averaged InSAR displacement transect with the modeled displacement transect at each time step and for each rheological setup by means of the RMSE (Tables S6–S13). We then calculated the averaged sum of the RMSE of all time steps (for each overpressure and rheological setup; Tables S14 and S15) to find three favored rheological conditions that yield the lowest RMSE. These results were used to identify the best rheological models to be subsequently tested with the linear pressurization assumption.

The linear pressure models (section 3.3.1) were then applied at the three favored rheological models. We followed the approach described in the previous paragraph to find the optimal solution that yields the overall lowest RMSE (RMSE for linear pressure models in Tables S16–S18). Figure S8 shows an illustrated example

between an instant and linear pressure model, the latter showing a better fit (for a single pixel, instead of all pixels in the transect) as evidenced by lower residuals.

4. Results

4.1. Observed Deformation and Analytical Mogi Model

We present the InSAR results in the form of averaged LOS velocity maps and displacement time series in Figures 1b and 1c. Positive LOS displacements (LOS decrease, red colors) represent ground movement toward the satellite (e.g., uplift), and negative LOS displacement (LOS increase, blue colors) represent ground movement away from the satellite (e.g., subsidence).

Our results do not show evident deformation prior to February 2010 (Figure 1b) but clearly reveal inflation during the period between February 2010 to March 2011 (Figure 1c), correlating with the period of increased seismicity, degassing, and ground temperatures. The strongest signal is centered over Taal volcano with an average LOS displacement of 11 cm. A subtle signal is also observed west of the shoreline of the caldera lake (Figure 1).

The best-fitting analytical point source is located beneath the NE quadrant of the main crater (Figures 1 and S9), centered at 3.1-km depth (95% confidence range of 0.9–5.3-km depth) below the summit, and with an RMSE of 17.9 mm (Table S4). Assuming a source radius of 1 km (section 3.3.1) and a shear modulus of 9.1 GPa (Table S5), the estimated volume change of $6.1 \times 10^6 \text{ m}^3$ (Table S4) would be equivalent to an overpressure of 17.6 MPa. This is within the range of overpressure values covered with the parametric sweeps for the numerical modeling. The modeled parameters with their trade-offs and confidence intervals are reported in Table S4 and Figure S10 in the supporting information.

4.2. Viscosity Models and Their Viscoelastic Response

The different compositional models and temperature distributions result in viscosity ranges of 10^{13} to $10^{25.1}$ Pa s at the magma reservoir-host rock interface, and $10^{12.8}$ to $10^{50.9}$ Pa s throughout the medium (Figure 3). Increasing temperatures with lower activation energy and Dorn parameter values (Figure 3d) yield the lowest calculated viscosities and therefore the models displaying the highest viscoelastic displacement, as can be seen in the time-dependent displacement curves for the eight model classes in Figure 4. Decreasing temperatures with increasing activation energy and Dorn parameter (Figure 3i) yield the highest calculated viscosities, making the time-dependent viscous effect on surface displacement negligible or absent in many models ($E_{A1} A_{D2}$, $E_{A2} A_{D1}$, and $E_{A2} A_{D2}$ with the cold geotherm, and $E_{A2} A_{D2}$ with the hot geotherms; Figure 4).

The time-dependent displacements for each of the eight viscoelastic models are shown for different source overpressures (applied instantaneously) in Figure 4. All models show the same initial displacements (from 3.2 to 16 cm) because of identical elastic properties (although this is difficult to see in Figure 4b, where displacements increase rapidly in the first day). In decreasing order, the $E_{A1} A_{D1}$ hot and cold models, and the $A_{D1} E_{A2}$ and $A_{D2} E_{A1}$ hot models (Figures 4a, 4b, 4d, and 4f) show from 8.7 to 0.5 cm viscoelastic displacement during the first year after source pressurization. The model with the lowest viscosities ($E_{A1} A_{D1}$ hot; Figure 3d) exhibits the fastest initial viscoelastic displacement rates (Figure 4b). The high-viscosity models (Figures 4c, 4e, 4g, and 4h) show no to negligible time-dependent behaviors.

The characteristic relaxation time will be proportional to $\eta/G\mu$ (section 3.3.4) and is an estimate of the time-scale needed to observe the full viscoelastic response with InSAR or any other geodetic technique. In order to view the complete viscoelastic response at the surface (directly above the pressurized reservoir) during the 1-year time interval of InSAR-observed deformation in this study and with an averaged shear modulus of ~ 9 GPa (Table S5), the averaged crustal viscosity above the reservoir would need to be in the order of 10^{17} Pa s. The only model that roughly meets this condition is the $E_{A1} A_{D1}$ hot model (Figures 3d and 4b). We show in panels a, d, and f of Figure 4 that viscoelastic deformation may still be measured for mediums with averaged crustal viscosities that are higher than 10^{17} Pa s (Figures 3c, 3f, and 3h), but the full viscoelastic response may occur over a timescale much larger than the InSAR observation period.

4.3. Best-Fitting Numerical Model

The three favored models of instantaneous pressurization suggest a source at 5-km depth with (1) 40 MPa of source overpressure within the viscoelastic configuration $E_{A1} A_{D2}$ of the hot model (RMSE of 19.73 mm), (2)

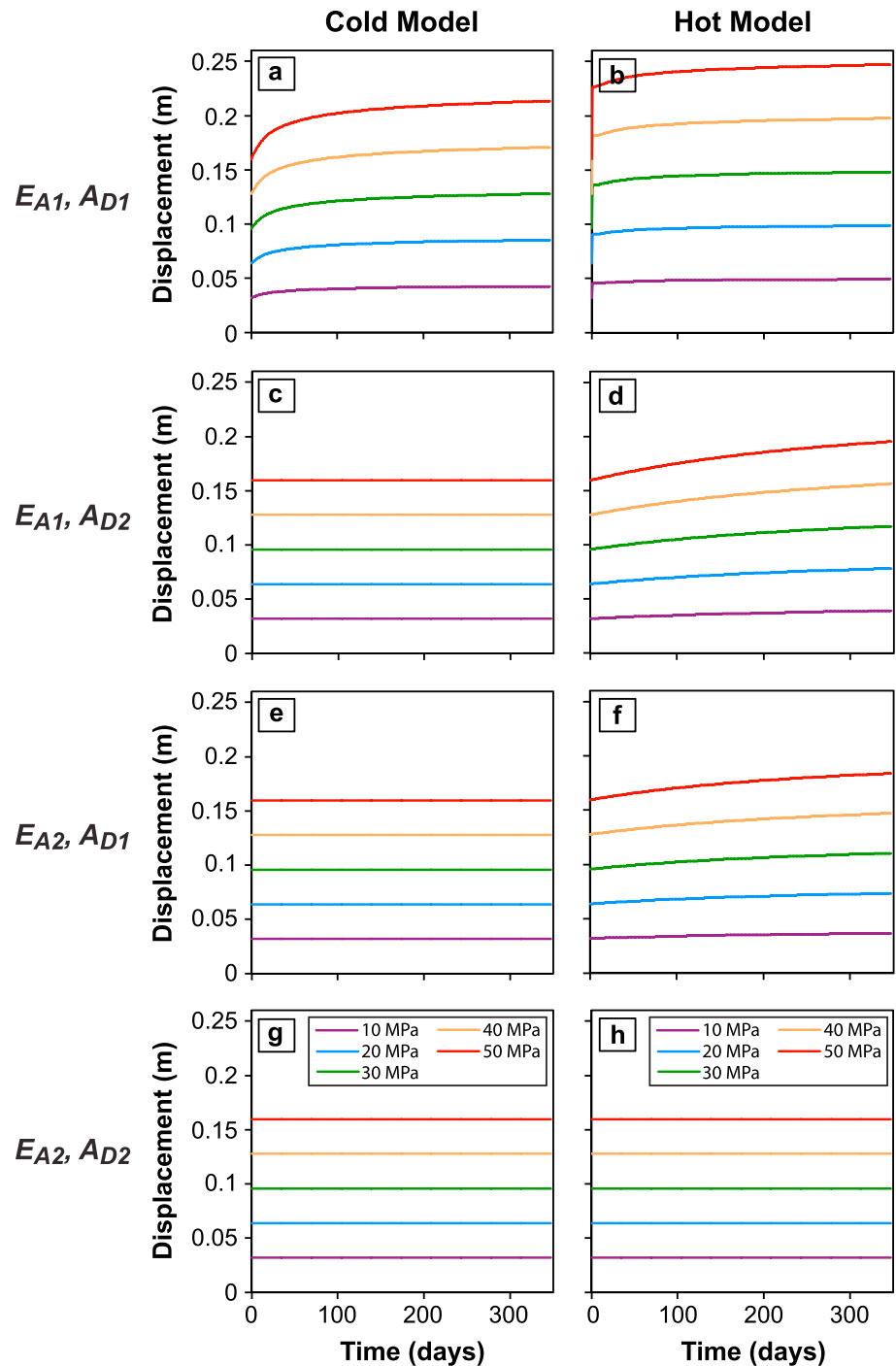


Figure 4. Time-dependent vertical surface displacement (directly above the source center) for the eight different viscoelastic models, for a spheroidal source (1-km radius) centered at 5-km depth and with instant overpressures of 10, 20, 30, 40, and 50 MPa.

30 MPa of source overpressure within the viscoelastic configuration $E_{A1} A_{D1}$ of the hot model (RMSE of 19.92 mm), and (3) 40 MPa of source overpressure within the viscoelastic configuration $E_{A1} A_{D1}$ of the cold model (RMSE of 19.92 mm). Figure 5 shows an example of the observed and modeled displacement spectrum resulting at the four different time steps for all rheological configurations (from an instant overpressure of 40 MPa at time 0). The linear pressure models (section 3.3.1) were then applied at these

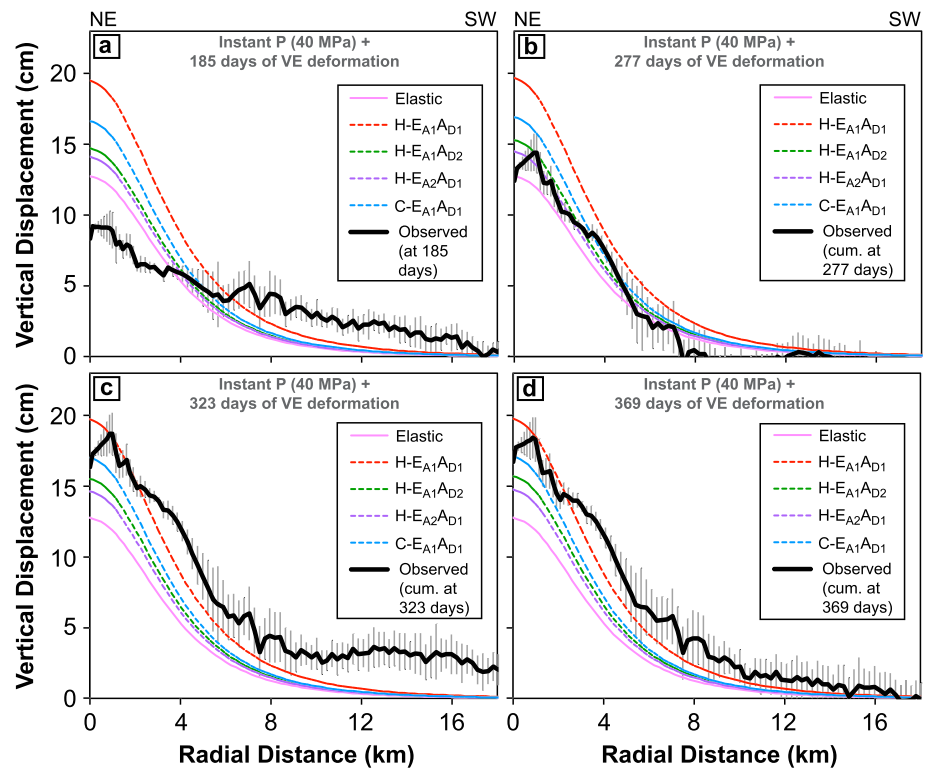


Figure 5. Observed and modeled vertical displacements (instant pressure assumption) as a function of radial distance from the source at (a) 185 days, (b) 277 days, (c) 323 days, and (d) 369 days for the given rheological configurations (for the source depth and overpressure, respectively, of 5 km and 40 MPa, of the favored instant pressure model). Black solid line: Observed cumulative displacement from averaged transects at each time step (from Figure S7). Gray error bars: Cumulative standard deviation. Pink solid line: Instantaneous, elastic deformation. Dashed lines: 185 to 369 days of viscoelastic deformation for four different rheological configurations that produce time-dependent surface deformation (Figures 4a, 4b, 4d, and 4f). H: Hot model; C: Cold model. Viscoelastic configurations with negligible time-dependent deformation ($E_{A1} A_{D2}$, $E_{A2} A_{D1}$, and $E_{A2} A_{D2}$ cold models, and $E_{A2} A_{D2}$ hot model) are also represented by the elastic model profile.

three favored viscoelastic medium characteristics (determined by the instant pressure model) to find the best-fitting solution, as mentioned in section 3.3.5.

The best-fitting forward numerical model is the viscoelastic configuration $E_{A1} A_{D1}$ of the hot model with a linear pressure increase of 40 MPa during 323 days. This configuration produces a maximum surface uplift of 19.23 cm during 323 days and an additional 0.23 cm by the last SAR acquisition, resulting from the source pressurization at 5-km depth and having an averaged RMSE of 15.06 mm (Figure 6 and Table S16). An overpressure of 40 MPa would be equivalent to a volume change of $1.38 \times 10^7 \text{ m}^3$, from the source radius of 1 km and the approximated shear modulus of 9.1 GPa (Table S5). Figures 6a, 6b, 6c, and 6d show the time series of the displacement transect for the best-fit model (at each time step), collocated with the observed displacement. Figure 6e shows the modeled displacement time series at the origin of the transect, collocated with the corresponding InSAR displacement time series (pixel over the analytical source). The rough fit between the modeled displacement to the observed InSAR displacement in Figure 6e is explained by a higher residual at the origin of the transect because the best-fit model was obtained for an averaged transect >15 km long (section 3.3.5), not for a single pixel with 30-m resolution.

5. Discussion

5.1. Deformation Source of the 2010–2011 Unrest

The best-fitting numerical model is consistent with previous observations of a shallow magmatic source beneath Taal volcano island, as summarized in the following. Previous GPS-derived measurements of the

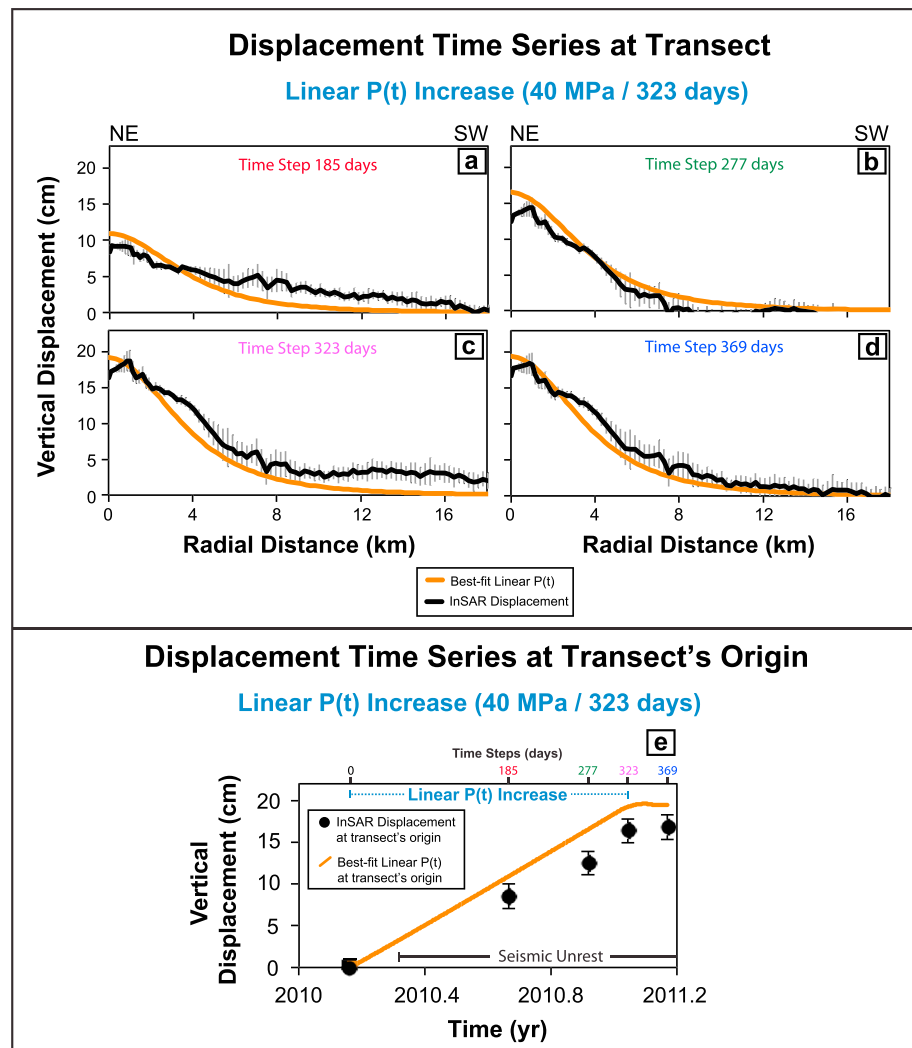


Figure 6. Time-dependent displacement at the surface of the $E_{A1} A_{D1}$ hot model, due to linear pressure increase of 40 MPa in 323 days from a source at 5-km depth (best-fitting solution). (a–d) Visual fit of the modeled (orange line) and observed (black line with error bars; from Figure 5) displacement transect at each time step. (e) Modeled displacement time series at the transect's origin (orange line), collocated with InSAR displacement time series for the pixel over the analytical source (black circles; see Figure 1 for location on map) during the period of deformation. Black error bars: Standard deviation of a nondeforming region with an area of 225 km², north of Taal Lake (centered at 14.2153°, 120.9320°). Seismic unrest started 26 April 2010 (Arpa et al., 2013).

inflationary and deflationary episodes of 1998, 1999, 2000, and 2005 events at Taal have estimated pressure sources beneath Taal volcano at 2- to 6-km depths (Bartel et al., 2003; Galgana et al., 2014; Lowry et al., 2001). Inflation has been attributed to a magmatic source and deflation to a shallower hydrothermal system (Bartel et al., 2003). A magnetotelluric resistivity study at Taal (Yamaya et al., 2013) revealed a large hydrothermal system at 1- to 4-km depths, and a high resistivity contrast at 4- to 6-km depths. The highly resistive region has been suggested to represent a density contrast where the formation of a magma reservoir would be favored (Yamaya et al., 2013).

All of these observations are consistent with a stationary shallow magmatic source overlain by a large hydrothermal system. Our best-fitting viscoelastic model further supports a shallow magmatic source at 5-km depth, indicating recharging of the shallow magma reservoir during the 2010–2011 deformation. The 2010–2011 unrest at Taal was also suggested to result from magmatic injection into a shallow reservoir as supported by the observed changes in gas emission rates and composition (Arpa et al., 2013). Moreover, our

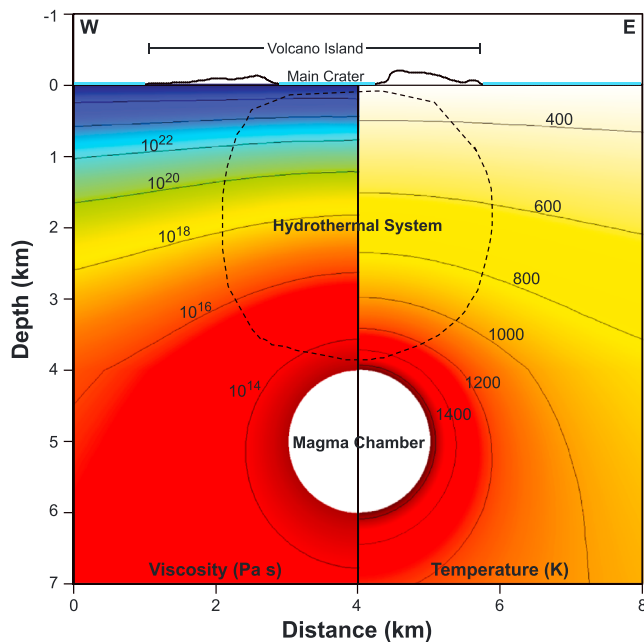


Figure 7. W-E cross section of Taal Volcano Island, showing (left) the viscosity distribution and (right) the temperature distribution for the best-fitting rheological configuration ($E_{A1} A_{D1}$ hot model). Black dashed line: Unconstrained shape of the hydrothermal reservoir. The cross section is centered over the origin of the modeled magma reservoir.

estimated volume change of $1.38 \times 10^7 \text{ m}^3$ (section 4.3) correlates with the estimated range of 10^5 – 10^7 m^3 of magma volume involved in the 2010–2011 swarm of long-period seismic events at Taal (Maeda et al., 2013). Our results also support the hot instead of the cold temperature model of the upper crust, in agreement with the reported temperatures of $>200 \text{ }^\circ\text{C}$ ($>473 \text{ K}$) of the hydrothermal system (Delmelle et al., 1998) above the magma source ($E_{A1} A_{D1}$ hot model; Figure 7).

Given the high temperatures of the upper crust at Taal, it is unlikely that deformation there is purely elastic, even if similar fits to the data could be obtained by the common trade-offs between source depth and overpressure. In Figure 4 we showed that for every additional 10 MPa of modeled overpressure in a source at 5-km depth and within an elastic medium with our seismically determined elastic properties, displacement increases by $\sim 3 \text{ cm}$ (initial displacements in Figure 4). An instant pressure of $\sim 60 \text{ MPa}$ (at 5 km) in this elastic medium would be required to reproduce the same displacement after ~ 1 year of viscoelastic response from 40 MPa of overpressure within the $E_{A1} A_{D1}$ hot model in Figure 4b. This shows that a purely elastic crust would require a larger overpressure to model the observed deformation, which could mislead to an overestimated volume change (in this case would result in an additional volume of $6.9 \times 10^6 \text{ m}^3$) and a misinterpretation of a magma reservoir closer to failure conditions (e.g., Albino et al., 2018).

The best analytical, instant pressure (numerical), and linear pressure rate (numerical) solutions, respectively, had RMSE estimates of 17.90, 19.73, and 15.06 mm). The linear pressure rate increase in a viscoelastic medium

model best explains the 2010 deformation at Taal while incorporating realistic representations of the rheological properties and time-dependent processes that are ignored by the commonly used analytical or numerical solutions of instant pressure.

5.2. Rheological Implications

The best-fitting viscoelastic model ($E_{A1} A_{D1}$ hot model) is in partial agreement with the expected rheological properties of the geologic setting and volcanic system at Taal, such as the high temperature estimates of the hydrothermal system above a magmatic source that result in a hot thermal gradient within the shallow crust. The activation energy and Dorn parameter of the best-fitting model matched that of a felsic crust, differing from the expectations of an intermediate crustal composition in the Philippines. Our results could be representative of the complexity within the rheological properties in a shallow volcanic system that is neither purely felsic nor intermediate, as explained in the following.

Vogel et al. (2006) noted the emplacement of silicic magmas all over the Macolod Corridor, an occurrence that is debated due to the lack of an old and evolved crust in the Macolod Corridor. They suggested it to result from partial melting of mantle-derived and evolved magmas that ponded and crystallized in the crust. The fact that drilling data at Mount Makiling in the Macolod Corridor revealed thick layers of silicic material in the upper crust (Vogel et al., 2006) and that some of the erupted lavas from Taal are dacitic in composition (Miklius et al., 1991) supports the presence of silicic material in the upper crust at Taal volcano island, consistent with the felsic compositional model of the best-fitting viscoelastic configuration ($E_{A1} A_{D1}$).

Alternatively, the large hydrothermal reservoir beneath Taal island could significantly alter the composition and properties of the uppermost crust due to presence of fluids, high temperatures, and alteration to clay minerals. Yamaya et al. (2013) suggested the possibility of alteration to clay minerals such as smectite at temperatures $<200 \text{ }^\circ\text{C}$ ($<473 \text{ K}$), and chlorite or illite at temperatures $>200 \text{ }^\circ\text{C}$ ($>473 \text{ K}$) within the hydrothermal reservoir beneath Taal volcano island. Activation energies ranging from 105 to 146 kJ/mol have been suggested for smectite to mixed illite/smectite layers at temperatures between $270 \text{ }^\circ\text{C}$ (543 K) and $350 \text{ }^\circ\text{C}$ (623 K; Roberson & Lahann, 1981), and these values correlate with those used to represent the felsic material constants and the temperatures of the hydrothermal reservoir at Taal that have been suggested by previous

studies. Our results could represent the complexity within the rheological properties in a shallow volcanic system that is neither purely felsic nor intermediate but altered.

Viscosities from the Arrhenius approach are approximated under the assumption that the experimentally determined material constants (e.g., Dorn parameter and Activation Energy; Kirby & Kronenberg, 1987) are true representations of material properties in the subsurface. However, it is important to note that the details on the conditions and assumptions about how the values of these constants were approximated and how they vary for crustal rocks under natural conditions are limited in the literature, particularly for the Dorn parameter. It has been suggested that the Dorn parameter values vary systematically depending on their elastic moduli (McLean & Hale, 1961; Tsenn & Carter, 1987). Therefore, it is a possibility that the typical values used as the material constant representing the Dorn parameter are not true representations of these crustal rocks within volcanic systems but could serve to compensate for possible variations of the elastic moduli or composition. Future viscoelastic models should account for a range of values to represent the Dorn parameter and not limit them to the typical representation of a felsic crust, as choosing between representing a felsic or intermediate crust would significantly alter the viscosity by an order of 10^4 Pa s and therefore the deformation results.

Nevertheless, the results (1) support the findings of previous studies that observed better data-model agreement by incorporation of more realistic subsurface representations and material properties (e.g., Hickey et al., 2016; Masterlark et al., 2016) than those represented by simple elastic half-space analytical solutions, (2) demonstrate that variability within all of the parameters used to calculate the viscosity significantly influences the resultant rheology of the host rock and therefore deformation, and (3) demonstrate that the best-fitting rheological scenario matches the previous multidisciplinary observations of the local geologic setting.

5.3. Limitations

Taal caldera is a large and long-lived magmatic system, supporting a significantly heated subsurface with rocks that become ductile (e.g., Bonafede et al., 1986; de Silva & Gregg, 2014; Dragoni & Magnanensi, 1989; Gregg et al., 2012; Jellinek & DePaolo, 2003; Newman et al., 2006). For this reason, a viscoelastic rheology provides a reasonable simplification for this geologic setting and was chosen for our model assumptions. Recent studies have shown the important contribution of thermoporoelastic effects in volcanoes with hydrothermal systems (e.g., Coco et al., 2016; Currenti et al., 2017; Currenti & Napoli, 2017; Hurwitz et al., 2007), which may also induce or partly explain the observed surface deformation at Taal. But including a thermoporoelastic rheology was out of the scope of our study and neglected in our model assumptions, because previous geochemical analysis supports magma recharging of the shallow magma storage region during the 2010–2011 unrest at Taal (Arpa et al., 2013), which supports inflation of the magma storage region.

The complex properties and processes occurring in a shallow hydrothermal system are difficult to constrain, vary in space and time, and can affect the temperature distribution in the subsurface (e.g., Currenti & Napoli, 2017; Hurwitz et al., 2007). These variations are neglected under the steady state temperature assumption; therefore, the temperature distributions presented here provide a first-order approximation.

We have approached the issue for a pressurized spherical reservoir, because the spatial deformation pattern appears to be circular. However, our deformation data are spatially limited by the lake surrounding Taal volcano. Thus, we did not address the possible effects from varying magma reservoir size and geometry, because there is no evidence in our data to justify adding these type of complexities to the model. We have also neglected variations and temperature dependency of the elastic parameters. The model results and overall deformation are highly dependent on the combination of all of these properties and interactions between the host rock and source. Therefore, our results represent the best-fitting solutions for the tested parameters and assumptions of the forward model.

Our deformation data at Taal were also limited due to the low temporal resolution of ALOS-1 InSAR image acquisitions. Inflation was observed at only four dates in ~ 1 year, which were used to constrain the time steps used for the data-model comparisons to identify the optimal solution. We acknowledge that other time steps could potentially lead to different results, which could be tested in future studies that have a higher temporal resolution data set. Additionally, time-dependent deformation cannot be discarded for the period after March 2011, correlating with the end of temporal coverage from the ALOS-1 deformation survey.

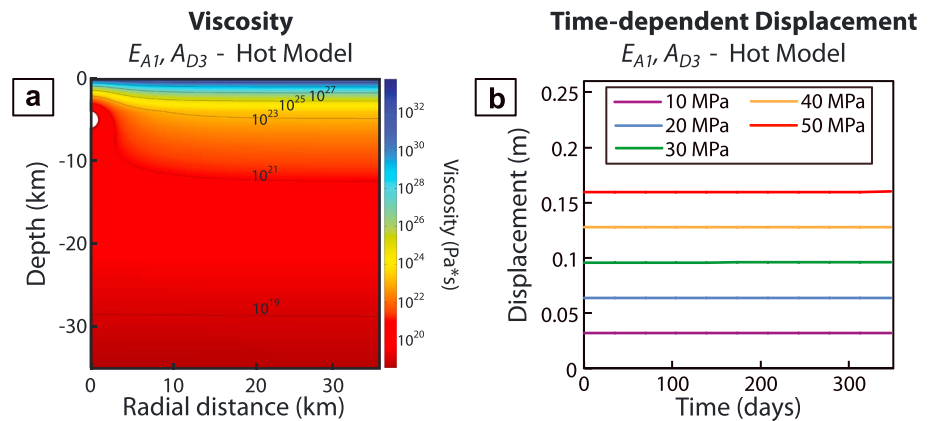


Figure 8. (a) Viscosity distribution calculated from the Arrhenius formulation, and (b) time-dependent vertical surface displacement directly over the source center for the $E_{A1} A_{D3}$ crustal parameter combination of a mafic crust experiment (see section 5.4). The spheroidal source (1-km radius) is centered at 5-km depth and with overpressures of 10, 20, 30, 40, and 50 MPa.

PHIVOLCS reported that a continuous GPS survey (unpublished) conducted at Taal Volcano island since February 2011 showed slight but steady inflation until August 2011.

5.4. Implications for Volcanoes With Mafic Compositions

In the sections above we have considered felsic to intermediate crustal compositions, which are appropriate for andesitic to rhyolitic volcanoes in island arc or continental arc settings. Basaltic volcanoes on hot spot oceanic islands such as in the Galapagos and in the Hawaiian Islands (e.g., Amelung et al., 2000; Baker & Amelung, 2012; Poland et al., 2012) or on island arcs, such as Okmok volcano (Lu & Dzurisin, 2014) can exhibit intereruption inflation of several tens of centimeters to several meters. At these volcanoes ground displacements are generally interpreted as changes in the magma reservoir volume or pressure. Here we adapt the models from Taal volcano for mafic compositions to investigate the viscoelastic response of basaltic volcanoes.

We use the same numerical models as before (1-km radius magma reservoir at 5-km depth) but with an activation energy of 260 kJ/mol (E_{A3}) and/or Dorn parameter of 3.2×10^{15} Pa s (A_{D3}) to represent the rheological configuration for a mafic crust (Ranalli & Murphy, 1987). A total of 10 model classes resulted from the possible viscosity parameter combinations that contain a mafic component ($E_{A1} A_{D3}$, $E_{A2} A_{D3}$, $E_{A3} A_{D1}$, $E_{A3} A_{D2}$, and $E_{A3} A_{D3}$ with the two thermal models). The viscosity ranges from $10^{17.8}$ to $10^{29.5}$ Pa s at the magma reservoir-host rock interface and from $10^{17.2}$ to $10^{60.2}$ Pa s throughout the medium (Figure S13). Figures 8a and 8b show the viscosity distribution for the $E_{A1} A_{D3}$ hot model and the corresponding displacement time series for different magma reservoir overpressures. The medium behaves elastically, as shown by the negligible time-dependent surface displacement for different magma reservoir overpressures (Figure 8b). The viscosity models for the other nine model configurations (Figure S13) are characterized by generally higher viscosities, implying an even smaller time-dependent viscoelastic response (RMSE estimates in Tables S6, S8, S10, S12, and S7, S9, S11, S13 demonstrate similarity, respectively, between elastic and viscoelastic responses of the models with mafic component).

These models suggest that for basaltic volcanoes in a mafic crust, time-dependent viscoelastic effects are so small that they can likely be neglected. Many basaltic volcanoes have shallower magma reservoirs than modeled here (e.g., 2- to 3-km depth below the surface at Sierra Negra and Kilauea volcanoes). The temperatures at these depths are smaller than at the modeled 5 km, suggesting an even smaller viscoelastic contribution.

6. Summary and Conclusions

InSAR data revealed significant uplift at Taal volcano during the 2010–2011 unrest, with an averaged LOS displacement of 11 cm at Taal volcano island. Deformation is explained by a time-dependent linear

pressure increase within a shallow magma reservoir at 5-km depth and in a viscoelastic medium. Viscoelastic modeling also supports the presence of the hot hydrothermal system above the magmatic source, supporting previous observations at Taal volcano. Viscoelastic deformation models that incorporate the characteristics of the local geologic setting provided significantly better results than simple elastic analytical solutions, and were invaluable to constrain realistic approximations of the rheological properties of the subsurface.

The material-dependent parameters (e.g., Dorn parameter and activation energy) for the viscosity calculations are commonly assumed constant in viscoelastic volcano deformation studies. Our results have important implications because we discussed and demonstrated their variability, its significant effects on determination of rheological characteristics, and its influence on surface deformation at different volcanic settings. Therefore, future viscoelastic models should account for these variabilities, as this information is vital for our better understanding of volcanic systems and needed for future research that focuses on assessing the potential for magma reservoir rupture and eruption.

Acknowledgments

The ALOS PALSAR data are copyright of the Japan Aerospace Exploration Agency (JAXA) and the Japanese Ministry of Economy, Trade, and Industry (METI). These data were made available by the UNAVCO Facility's SAR data sharing system. InSAR time series analysis and post-processing was conducted using the PySAR software, developed by Heresh Fattahi and Yunjun Zhang (<https://github.com/yunjunz/PySAR>). The University of Miami's GeodMod software was used for the analytical modeling. InSAR data products are available at <http://insar-maps.miami.edu/>. We thank NSF for support through the EAR-1345129 grant. We also thank Paul Tregoning, Yosuke Aoki, James Hickey, and two anonymous reviewers for their detailed and constructive suggestions that lead to major improvements in our paper.

References

- Adelinet, M., Fortin, J., Guéguen, Y., Schubnel, A., & Geoffroy, L. (2010). Frequency and fluid effects on elastic properties of basalt: Experimental investigations. *Geophysical Research Letters*, *37*, L02303. <https://doi.org/10.1029/2009GL041660>
- Albino, F., Amelung, F., & Gregg, P. (2018). The role of pore fluid pressure on the failure of magma reservoirs: Insights from Indonesian and Aleutian arc volcanoes. *Journal of Geophysical Research: Solid Earth*, *123*, 1328–1349. <https://doi.org/10.1002/2017JB014523>
- Amelung, F., Jónsson, S., Zebker, H., & Segall, P. (2000). Widespread uplift and 'trapdoor' faulting on Galápagos volcanoes observed with radar interferometry. *Nature*, *407*(6807), 993–996. <https://doi.org/10.1038/35039604>
- Arpa, M. C., Hernández, P. A., Padrón, E., Reniva, P., Padilla, G. D., Bariso, E., Melián, G. V., et al. (2013). Geochemical evidence of magma intrusion inferred from diffuse CO₂ emissions and fumarole plume chemistry: The 2010–2011 volcanic unrest at Taal volcano, Philippines. *Bulletin of Volcanology*, *75*(10), 747. <https://doi.org/10.1007/s00445-013-0747-9>
- Baker, S., & Amelung, F. (2012). Top-down inflation and deflation at the summit of Kilauea volcano, Hawai'i observed with InSAR. *Journal of Geophysical Research*, *117*, B12406. <https://doi.org/10.1029/2011JB009123>
- Bartel, B. A., Hamburger, M. W., Meertens, C. M., Lowry, A. R., & Corpuz, E. (2003). Dynamics of active magmatic and hydrothermal systems at Taal Volcano, Philippines, from continuous GPS measurements. *Journal of Geophysical Research*, *108*(B10), 2475. <https://doi.org/10.1029/2002JB002194>
- Berardino, P., Fornaro, G., Lanari, R., & Sansosti, E. (2002). A new algorithm for surface deformation monitoring based on small baseline differential SAR interferograms. *IEEE Transactions on Geoscience and Remote Sensing*, *40*(11), 2375–2383. <https://doi.org/10.1109/TGRS.2002.803792>
- Besana, G. M., Shibutani, T., Hirano, N., Ando, M., Bautista, B., Narag, I., & Punongbayan, R. S. (1995). The shear wave velocity structure of the crust and uppermost mantle beneath Tagaytay, Philippines inferred from receiver function analysis. *Geophysical Research Letters*, *22*(23), 3143–3146. <https://doi.org/10.1029/95GL03319>
- Bonafede, M., Dragoni, M., & Quarenì, F. (1986). Displacement and stress fields produced by a Centre of dilation and by a pressure source in a viscoelastic half-space: Application to the study of ground deformation and seismic activity at Campi Flegrei, Italy. *Geophysical Journal of the Royal Astronomical Society*, *87*(2), 455–485. <https://doi.org/10.1111/j.1365-246X.1986.tb06632.x>
- Brocher, T. M. (2005). Empirical relations between elastic wavespeeds and density in the Earth's crust. *Bulletin of the Seismological Society of America*, *95*(6), 2081–2092. <https://doi.org/10.1785/0120050077>
- Brooks, B. A., & Frazer, L. N. (2005). Importance reweighting reduces dependence on temperature in Gibbs samplers: An application to the coseismic geodetic inverse problem. *Geophysical Journal International*, *161*(1), 12–20. <https://doi.org/10.1111/j.1365-246X.2005.02573.x>
- Cayol, V., & Cornet, F. H. (1998). Effects of topography on the interpretation of the deformation field of prominent volcanoes—Application to Etna. *Geophysical Research Letters*, *25*(11), 1979–1982. <https://doi.org/10.1029/98GL51512>
- Chen, C. W., & Zebker, H. A. (2001). Two-dimensional phase unwrapping with use of statistical models for cost functions in nonlinear optimization. *Journal of the Optical Society of America. A, Optics, Image Science, and Vision*, *18*(2), 338–351. <https://doi.org/10.1364/JOSAA.18.000338>
- Christensen, R. M. (1971). *Theory of viscoelasticity: An introduction* (p. 245). New York and London: Academic Press.
- Ciccotti, M., & Mulargia, F. (2004). Differences between static and dynamic elastic moduli of a typical seismogenic rock. *Geophysical Journal International*, *157*(1), 474–477. <https://doi.org/10.1111/j.1365-246X.2004.02213.x>
- Clauser, C., & Huenges, E. (2013). Thermal conductivity of rocks and minerals. In *Rock physics and phase relations* (pp. 105–126), Washington, DC: American Geophysical Union. <https://doi.org/10.1029/RF003p0105>
- Coco, A., Gottsmann, J., Whitaker, F., Rust, A., Currenti, G., Jasim, A., & Bunney, S. (2016). Numerical models for ground deformation and gravity changes during volcanic unrest: Simulating the hydrothermal system dynamics of a restless caldera. *Solid Earth*, *7*(2), 557–577. <https://doi.org/10.5194/se-7-557-2016>
- Currenti, G., & Napoli, R. (2017). Learning about hydrothermal volcanic activity by modeling induced geophysical changes. *Frontiers in Earth Science*, *5*(41). <https://doi.org/10.3389/feart.2017.00041>
- Currenti, G., Napoli, R., Coco, A., & Privitera, E. (2017). Effects of hydrothermal unrest on stress and deformation: Insights from numerical modeling and application to Vulcano Island (Italy). *Bulletin of Volcanology*, *79*(4), 28. <https://doi.org/10.1007/s00445-017-1110-3>
- Currenti, G., & Williams, C. A. (2014). Numerical modeling of deformation and stress fields around a magma chamber: Constraints on failure conditions and rheology. *Physics of the Earth and Planetary Interiors*, *226*, 14–27. <https://doi.org/10.1016/j.pepi.2013.11.003>
- de Silva, S. L., & Gregg, P. M. (2014). Thermomechanical feedbacks in magmatic systems: Implications for growth, longevity, and evolution of large caldera-forming magma reservoirs and their supereruptions. *Journal of Volcanology and Geothermal Research*, *282*, 77–91. <https://doi.org/10.1016/j.jvolgeores.2014.06.001>
- Del Negro, C., Currenti, G., & Scandura, D. (2009). Temperature-dependent viscoelastic modeling of ground deformation: Application to Etna volcano during the 1993–1997 inflation period. *Physics of the Earth and Planetary Interiors*, *172*(3–4), 299–309. <https://doi.org/10.1016/j.pepi.2008.10.019>

- Delmelle, P., Kusakabe, M., Bernard, A., Fischer, T., de Brouwer, S., & del Mundo, E. (1998). Geochemical and isotopic evidence for seawater contamination of the hydrothermal system of Taal volcano, Luzon, the Philippines. *Bulletin of Volcanology*, *59*(8), 562–576. <https://doi.org/10.1007/s004450050210>
- Delos Reyes, P. J., Bornas, M. A. V., Dominey-Howes, D., Pidlaon, A. C., Magill, C. R., & Solidum, J. R. U. (2018). A synthesis and review of historical eruptions at Taal volcano, Southern Luzon, Philippines. *Earth-Science Reviews*, *177*, 565–588. <https://doi.org/10.1016/j.earscirev.2017.11.014>
- Dragoni, M., & Magnanensi, C. (1989). Displacement and stress produced by a pressurized, spherical magma chamber, surrounded by a viscoelastic shell. *Physics of the Earth and Planetary Interiors*, *56*(3-4), 316–328. [https://doi.org/10.1016/0031-9201\(89\)90166-0](https://doi.org/10.1016/0031-9201(89)90166-0)
- Gaeta, F. S., De Natale, G., Peluso, F., Mastrolorenzo, G., Castagnolo, D., Troise, C., Pingue, F., et al. (1998). Genesis and evolution of unrest episodes at Campi Flegrei caldera: The role of thermal fluid-dynamical processes in the geothermal system. *Journal of Geophysical Research*, *103*(B9), 20,921–20,933. <https://doi.org/10.1029/97JB03294>
- Galgana, G. A., Newman, A. V., Hamburger, M. W., & Solidum, R. U. (2014). Geodetic observations and modeling of time-varying deformation at Taal volcano, Philippines. *Journal of Volcanology and Geothermal Research*, *271*, 11–23. <https://doi.org/10.1016/j.jvolgeores.2013.11.005>
- Global Volcanism Program (2013). Database information. In E. Venzke (Ed.), *Volcanoes of the world*. Smithsonian Institution. <https://doi.org/10.5479/si.GVP.VOTW4-2013>
- Goldstein, R. M., & Werner, C. L. (1998). Radar interferogram filtering for geophysical applications. *Geophysical Research Letters*, *25*(21), 4035–4038. <https://doi.org/10.1029/1998GL900033>
- Gregg, P. M., de Silva, S. L., Grosfils, E. B., & Parmigiani, J. P. (2012). Catastrophic caldera-forming eruptions: Thermomechanics and implications for eruption triggering and maximum caldera dimensions on earth. *Journal of Volcanology and Geothermal Research*, *241*–242, 1–12. <https://doi.org/10.1016/j.jvolgeores.2012.06.009>
- Gudmundsson, A. (1990). Emplacement of dikes, sills and crustal magma chambers at divergent plate boundaries. *Tectonophysics*, *176*(3-4), 257–275. [https://doi.org/10.1016/0040-1951\(90\)90073-H](https://doi.org/10.1016/0040-1951(90)90073-H)
- Hanssen, R. F. (2001). *Radar interferometry: Data interpretation and error analysis*. Dordrecht, Netherlands: Springer Science & Business Media. <https://doi.org/10.1007/0-306-47633-9>
- Hickey, J., Gottsmann, J., & Mothes, P. (2015). Estimating volcanic deformation source parameters with a finite element inversion: The 2001–2002 unrest at Cotopaxi volcano, Ecuador. *Journal of Geophysical Research: Solid Earth*, *120*, 1473–1486. <https://doi.org/10.1002/2014JB011731>
- Hickey, J., Gottsmann, J., Nakamichi, H., & Iguchi, M. (2016). Thermomechanical controls on magma supply and volcanic deformation: Application to Aira caldera, Japan. *Scientific Reports*, *6*(1), 32691. <https://doi.org/10.1038/srep32691>
- Hickey, J., Gottsmann, J., & Potro, R. (2013). The large-scale surface uplift in the Altiplano-Puna region of Bolivia: A parametric study of source characteristics and crustal rheology using finite element analysis. *Geochemistry, Geophysics, Geosystems*, *14*, 540–555. <https://doi.org/10.1002/ggge.20057>
- Hurwitz, D. M., Long, S. M., & Grosfils, E. B. (2009). The characteristics of magma reservoir failure beneath a volcanic edifice. *Journal of Volcanology and Geothermal Research*, *188*(4), 379–394. <https://doi.org/10.1016/j.jvolgeores.2009.10.004>
- Hurwitz, S., Christiansen, L. B., & Hsieh, P. A. (2007). Hydrothermal fluid flow and deformation in large calderas: Inferences from numerical simulations. *Journal of Geophysical Research*, *112*, B02206. <https://doi.org/10.1029/2006JB004689>
- Jellinek, A. M., & DePaolo, D. J. (2003). A model for the origin of large silicic magma chambers: Precursors of caldera-forming eruptions. *Bulletin of Volcanology*, *65*(5), 363–381. <https://doi.org/10.1007/s00445-003-0277-y>
- Kirby, S. H., & Kronenberg, A. K. (1987). Rheology of the lithosphere: Selected topics. *Reviews of Geophysics*, *25*(6), 1219–1244. <https://doi.org/10.1029/RG025i006p01219>
- Le Mével, H., Gregg, P. M., & Feigl, K. L. (2016). Magma injection into a long-lived reservoir to explain geodetically measured uplift: Application to the 2007–2014 unrest episode at Laguna del Maule volcanic field, Chile. *Journal of Geophysical Research: Solid Earth*, *121*, 6092–6108. <https://doi.org/10.1002/2016JB013066>
- Lipman, P. W. (1997). Subsidence of ash-flow calderas: Relation to caldera size and magma-chamber geometry. *Bulletin of Volcanology*, *59*(3), 198–218. <https://doi.org/10.1007/s004450050186>
- Lisowski, M. (2006). Analytical volcano deformation source models, in *Volcano deformation: Geodetic monitoring techniques* (pp. 279–304). Berlin: Springer. https://doi.org/10.1007/978-3-540-49302-0_8
- Lowry, A. R., Hamburger, M. W., Meertens, C. M., & Ramos, E. G. (2001). GPS monitoring of crustal deformation at Taal volcano, Philippines. *Journal of Volcanology and Geothermal Research*, *105*(1-2), 35–47. [https://doi.org/10.1016/S0377-0273\(00\)00238-9](https://doi.org/10.1016/S0377-0273(00)00238-9)
- Lu, Z., & Dzurisin, D. (2014). *InSAR imaging of Aleutian volcanoes: Monitoring a volcanic arc from space* (1st ed.). Berlin: Springer. <https://doi.org/10.1007/978-3-642-00348-6>
- Maeda, Y., Kumagai, H., Lacson, R., Figueroa, M. S., & Yamashina, T. (2013). Source process of long-period seismic events at Taal volcano, Philippines: Vapor transportation and condensation in a shallow hydrothermal fissure. *Journal of Geophysical Research: Solid Earth*, *118*, 2832–2846. <https://doi.org/10.1002/jgrb.50205>
- Masterlark, T. (2007). Magma intrusion and deformation predictions: Sensitivities to the Mogi assumptions. *Journal of Geophysical Research*, *112*, B06419. <https://doi.org/10.1029/2006JB004860>
- Masterlark, T., Donovan, T., Feigl, K. L., Haney, M., Thurber, C. H., & Tung, S. (2016). Volcano deformation source parameters estimated from InSAR: Sensitivities to uncertainties in seismic tomography. *Journal of Geophysical Research: Solid Earth*, *121*, 3002–3016. <https://doi.org/10.1002/2015JB012656>
- Masterlark, T., Haney, M., Dickinson, H., Fournier, T., & Searcy, C. (2010). Rheologic and structural controls on the deformation of Okmok volcano, Alaska: FEMs, InSAR, and ambient noise tomography. *Journal of Geophysical Research*, *115*, B02409. <https://doi.org/10.1029/2009JB006324>
- McBirney, A. R., & Murase, T. (1984). Rheological properties of magmas. *Annual Review of Earth and Planetary Sciences*, *12*(1), 337–357. <https://doi.org/10.1146/annurev.ea.12.050184.002005>
- McLean, D., & Hale, K. F. (1961). The stress sensitivity of creep. *Structural Properties in Creep*, 70.
- McTigue, D. F. (1987). Elastic stress and deformation near a finite spherical magma body: Resolution of the point source paradox. *Journal of Geophysical Research*, *92*(B12), 12,931–12,940. <https://doi.org/10.1029/JB092iB12p12931>
- Meissner, R., & Tanner, B. (1992). Crustal viscosities and seismic velocities. *Physics of the Earth and Planetary Interiors*, *69*(3-4), 252–256. [https://doi.org/10.1016/0031-9201\(92\)90143-J](https://doi.org/10.1016/0031-9201(92)90143-J)

- Miklius, A., Flower, M. F. J., Huijsmans, J. P. P., Mukasa, S. B., & Castillo, P. (1991). Geochemistry of lavas from Taal volcano, southwestern Luzon, Philippines: Evidence for multiple magma supply systems and mantle source heterogeneity. *Journal of Petrology*, *32*(3), 593–627. <https://doi.org/10.1093/petrology/32.3.593>
- Mogi, K. (1958). Relations between the eruptions of various volcanoes and the deformations of the ground surfaces around them. *Bulletin. Earthquake Research Institute, University of Tokyo*, *36*, 99–134.
- Morales Rivera, A. M., Amelung, F., & Mothes, P. (2016). Volcano deformation survey over the Northern and Central Andes with ALOS InSAR time series. *Geochemistry, Geophysics, Geosystems*, *17*, 2869–2883. <https://doi.org/10.1002/2016GC006393>
- Morgan, J. P., & Chen, Y. J. (1993). The genesis of oceanic crust: Magma injection, hydrothermal circulation, and crustal flow. *Journal of Geophysical Research*, *98*(B4), 6283–6297. <https://doi.org/10.1029/92JB02650>
- Morgan, P., Blackwell, D. D., Spafford, R. E., & Smith, R. B. (1977). Heat flow measurements in Yellowstone Lake and the thermal structure of the Yellowstone caldera. *Journal of Geophysical Research*, *82*(26), 3719–3732. <https://doi.org/10.1029/JB082i026p03719>
- Newman, A. V., Dixon, T. H., & Gourmelen, N. (2006). A four-dimensional viscoelastic deformation model for Long Valley caldera, California, between 1995 and 2000. *Journal of Volcanology and Geothermal Research*, *150*(1–3), 244–269. <https://doi.org/10.1016/j.jvolgeores.2005.07.017>
- Pepe, A., & Lanari, R. (2006). On the extension of the minimum cost flow algorithm for phase unwrapping of multitemporal differential SAR interferograms. *IEEE Transactions on Geoscience and Remote Sensing*, *44*(9), 2374–2383. <https://doi.org/10.1109/TGRS.2006.873207>
- Poland, M. P., Miklius, A., Jeff Sutton, A., & Thornber, C. R. (2012). A mantle-driven surge in magma supply to Kilauea volcano during 2003–2007. *Nature Geoscience*, *5*(4), 295–300. <https://doi.org/10.1038/ngeo1426>
- Ranalli, G., & Murphy, D. C. (1987). Rheological stratification of the lithosphere. *Tectonophysics*, *132*(4), 281–295. [https://doi.org/10.1016/0040-1951\(87\)90348-9](https://doi.org/10.1016/0040-1951(87)90348-9)
- Roberson, H. E., & Lahann, R. W. (1981). Smectite to Illite conversion rates: Effects of solution chemistry. *Clays and Clay Minerals*, *29*(2), 129–135. <https://doi.org/10.1346/CCMN.1981.0290207>
- Roche, O., Druitt, T. H., & Merle, O. (2000). Experimental study of caldera formation. *Journal of Geophysical Research*, *105*(B1), 395–416. <https://doi.org/10.1029/1999JB900298>
- Rosen, P. A., Hensley, S., Peltzer, G., & Simons, M. (2004). Updated repeat orbit interferometry package released. *Eos, Transactions American Geophysical Union*, *85*(5), 47–47. <https://doi.org/10.1029/2004EO050004>
- Rothstein, D. A., and C. E. Manning (2003). Geothermal gradients in continental magmatic arcs: Constraints from the eastern peninsular ranges batholith, Baja California, México, Special Papers-Geological Society of America, 337-354.
- Segall, P. (2016). Reprersurization following eruption from a magma chamber with a viscoelastic aureole. *Journal of Geophysical Research: Solid Earth*, *121*, 8501–8522. <https://doi.org/10.1002/2016JB013597>
- Sparks, R. S. J. (2003). Forecasting volcanic eruptions. *Earth and Planetary Science Letters*, *210*(1–2), 1–15. [https://doi.org/10.1016/S0012-821X\(03\)00124-9](https://doi.org/10.1016/S0012-821X(03)00124-9)
- Stolper, E. M., DePaolo, D. J., & Thomas, D. M. (2009). Deep drilling into a mantle plume volcano: The Hawaii scientific drilling project. *Scientific Drilling*, *7*, 4–14. <https://doi.org/10.2204/iodp.sd.7.02.2009>
- Tsenn, M. C., & Carter, N. L. (1987). Upper limits of power law creep of rocks. *Tectonophysics*, *136*(1–2), 1–26. [https://doi.org/10.1016/0040-1951\(87\)90332-5](https://doi.org/10.1016/0040-1951(87)90332-5)
- Vogel, T. A., Flood, T. P., Patino, L. C., Wilmot, M. S., Maximo, R. P. R., Arpa, C. B., Arcilla, C. A., et al. (2006). Geochemistry of silicic magmas in the Macolod corridor, SW Luzon, Philippines: Evidence of distinct, mantle-derived, crustal sources for silicic magmas. *Contributions to Mineralogy and Petrology*, *151*(3), 267–281. <https://doi.org/10.1007/s00410-005-0050-7>
- Waples, D. W., & Waples, J. S. (2004). A review and evaluation of specific heat capacities of rocks, minerals, and subsurface fluids. Part 1: Minerals and nonporous rocks. *Natural Resources Research*, *13*(2), 97–122. <https://doi.org/10.1023/B:NARR.0000032647.41046.e7>
- Wauthier, C., Cayol, V., Kervyn, F., & d'Oreye, N. (2012). Magma sources involved in the 2002 Nyiragongo eruption, as inferred from an InSAR analysis. *Journal of Geophysical Research*, *117*, B05411. <https://doi.org/10.1029/2011JB008257>
- Werner, C., U. Wegmüller, T. Strozzi, and A. Wiesmann (2000). Gamma SAR and interferometric processing software, Proceedings of the ERS-ENVISAT Symposium, 16–20 October, Gothenburg, Sweden.
- Yamaya, Y., Alanis, P. K. B., Takeuchi, A., Cordon, J. M., Mogi, T., Hashimoto, T., Sasai, Y., et al. (2013). A large hydrothermal reservoir beneath Taal volcano (Philippines) revealed by magnetotelluric resistivity survey: 2D resistivity modeling. *Bulletin of Volcanology*, *75*(7), 729. <https://doi.org/10.1007/s00445-013-0729-y>
- You, S. H., Gung, Y., Lin, C. H., Konstantinou, K. I., Chang, T. M., Chang, E. T. Y., & Solidum, R. (2013). A preliminary seismic study of Taal volcano, Luzon Island Philippines. *Journal of Asian Earth Sciences*, *65*, 100–106. <https://doi.org/10.1016/j.jseas.2012.10.027>
- Zhao, W., Amelung, F., Doin, M.-P., Dixon, T. H., Wdowinski, S., & Lin, G. (2016). InSAR observations of lake loading at Yangzhuoyong Lake, Tibet: Constraints on crustal elasticity. *Earth and Planetary Science Letters*, *449*, 240–245. <https://doi.org/10.1016/j.epsl.2016.05.044>